SUPPLEMENTARY INFORMATION

Supplementary Methods

Age control of GeoB9501-4/5

The age model for multicore GeoB9501-4 and gravity core GeoB9501-5 was developed using a combination of two independent radiometric methods, i.e., $^{210}Pb_{xs}$- and ^{137}Cs-measurements applying the constant rate of supply (CRS) model[31], and AMS radiocarbon dating of planktic foraminifera (Supplementary Table 1). The details of the $^{210}Pb_{xs}$ and ^{137}Cs gamma spectroscopic measurements are described elsewhere[32,33]. Additionally, the self attenuation correction for low-energy ^{210}Pb (45.6 keV, I_γ 4.25%) for the multicore GeoB9501-4, necessary due to varying sample size, was calculated using a modification of the method described in Hurtado et al. (ref. 34), combining both experimental measurements and mathematical Monte Carlo (MC) simulations. In this study, the full-energy peak efficiencies for samples with zero density with different sample heights were generated using the MC based LabSOCS Genie 2000 calibration tool[35]. ^{210}Pb and ^{137}Cs were also measured for the associated gravity core GeoB9501-5. Here, due to constant geometry of the samples, no individual self-absorbtion correction was applied for ^{210}Pb. Depth matching of the gravity core and the multicore was performed using the corresponding $^{210}Pb_{xs}$ and ^{137}Cs profiles. The onset of ^{137}Cs corresponds to a depth of 29.5 cm in multicore GeoB9501-4 and to a depth of 8 cm in gravity core GeoB9501-5. Hence, about 21.5 cm of sediment material was lost during gravity coring (Supplementary Figure 1).

The availability of a $^{210}Pb_{xs}$-based age model for the multicore spanning the time period between 1915 and 2005 CE allowed the estimation of the local radiocarbon reservoir age using the AMS ^{14}C-date of a foraminifera sample from the bottom of a parallel core (45.5 cm) from the same multicorer cast. From the $^{210}Pb_{xs}$-based age model, we estimate that this core depth corresponds to about 1907 CE. The AMS-measurement for sample KIA35172 performed in 2008 yielded a fMC value of 0.9235 ±0.0036, which was converted to $\Delta^{14}C$=-82.956‰ using:

$$(1) \qquad \Delta^{14}C\ (‰) = (fMC / e^{(t-1950/8267)} -1) * 1000$$

where t is the year of measurement. Subsequently, the radiocarbon concentration of the sample at the time of deposition (initial $\Delta^{14}C$) was determined using:

(2) $\Delta^{14}C_{initial}$ (‰) = (($\Delta^{14}C$/1000+1)*$e^{(\lambda\Delta t)}$-1)*1000

where λ is the decay constant (ln(2)/5730 yr) and Δt is the time elapsed between the year of deposition and the year of measurement in years. This initial radiocarbon concentration can be converted into the reservoir age (R) using a rearrangement of (1) given as:

(3) fMC = ($\Delta^{14}C_{initial}$/1000+1) * $e^{(t-1950/8267)}$

and

(4) R = -8033 * ln(fMC).

For GeoB9501-4 we thus determined a reservoir age for the early 20th century of R = 541 yr. This reservoir age (ΔR=140 years) was used for calibration of the AMS radiocarbon dates of gravity core GeoB9501-4. We assumed a constant reservoir age throughout the time period covered by the sediment record. Radiocarbon ages were converted into calibrated 2σ calendar age ranges using the online calibration tool Calib 5.0.2 (http://radiocarbon.pa.qub.ac.uk /calib/calib.html) with the MARINE04 calibration curve and an additional local reservoir effect of 140 (± 100) years. Two radiocarbon ages were not included in the final age model because of questions concerning their fidelity. The radiocarbon age at 52 cm stems from the Little Ice Age for which models suggest a considerably higher reservoir effect for the core location (see ref. 36 and http://www.reservoirage.uni-bremen.de) and where a plateau in the calibration curve produces ambiguous results. The age at the base of the gravity core at 530 cm (not plotted in Supplementary Figure 2) was not included because of possible disturbance and potential inclusion of older material from the core catcher.

To construct a continuous depth-age model for the multicore and gravity core, a weighted fourth-order polynomial function was fitted to the pooled $^{210}Pb_{xs}$ and calibrated radiocarbon ages in a least-squares sense. Each point was weighted by σ^{-2}, where σ represents

the standard deviation of the point's age distribution. Assigning d to represent the composite core depth in centimeters the function to calculate the age A in yrs CE is given by:

$$A = -8.625032 \times 10^{-8} d^4 + 7.714495 \times 10^{-5} d^3 - 0.0248636 d^2 - 1.378884 d + 2.007679 \times 10^3$$

The uncertainties on the individual ages were transformed into errors on the weighted polynomial coefficients[37,38]. To determine a continuous sedimentation rate the reciprocal of the derivative of the weighted polynomial was calculated by a linear transform applied to the polynomial coefficients[38]. The same transform also allowed the errors on the polynomial coefficients to be mapped to provide a $\pm 2\sigma$ error envelope on the sedimentation rate (Supplementary Figure 2). All composite records have been constructed by using the entire record of the multicore and the record of the gravity core from the bottom age of the multicore downwards.

Supplementary Table S1: Radiocarbon age control points at site GeoB9501. Samples given with single depths denote depth intervals sampled with cut syringes of about 1.5 cm diameter centred over the given depth.

Depth (cm)	Core (GeoB)	Lab Code	Conv. Age (yr BP)	Age Range (2σ, CE)		
45-46	9501-4	KIA 35172*	640 ± 30 BP		-	
4-5	9501-5	KIA 32642**	-30 ± 70 BP		-	
52	9501-5	Poz-31132***	910 ± 40 BP	1348	–	1730
120	9501-5	KIA 3743	1040 ± 30 BP	1289	–	1640
202	9501-5	KIA 3744	1440 ± 30 BP	894	–	1299
254	9501-5	KIA 3745	1655 ± 30 BP	668	–	1089
350	9501-5	KIA 3746	2195 ± 30 BP	82	–	571
443	9501-5	KIA 3747	2675 ± 35 BP	-522	–	33
524-528	9501-5	KIA 32641	3540 ± 45 BP	-1581	–	-1013
530	9501-5	KIA 3748****	4130 ± 40 BP		-	

* Radiocarbon age from base of parallel core from multicore GeoB9501-4 used to derive reservoir age

** Radiocarbon age from 4-5 cm depth in gravity core GeoB9501-5 biased by bomb radiocarbon

*** Not included into the age model because of a larger reservoir age during the Little Ice Age (see text Age Control of GeoB9501-4/5)

**** Not included into the age model because of disturbance and potential inclusion of older material around the core catcher

Supplementary Table S2: Opal content for selected depths in core GeoB9501 measured by automated leaching[39]. Single depths denote depth intervals sampled with cut syringes of about 1.5 cm diameter centred over the given depth.

Depth (cm)	Core (GeoB)	Opal Content (wt %)
2-3	9501-4	1.30
20-21	9501-4	1.75
40-41	9501-4	0.50
76	9501-5	1.18
102	9501-5	1.71
134	9501-5	0.55
186	9501-5	1.76
254	9501-5	4.70
304	9501-5	1.89
344	9501-5	0.69
432	9501-5	0.78
456	9501-5	0.84
508	9501-5	2.37

Determination of grain size and bulk elemental concentrations

Grain size on the terrigenous fraction was determined with a Coulter Laser Particle Sizer LS200 every 2 cm downcore in the gravity core GeoB9501-5 and every cm in multicore GeoB9501-4. The pre-treatment steps to remove different biogenic constituents are described elsewhere[40].

Element concentrations were determined on 53 sediment samples from gravity core GeoB9501-5 and on 42 sediment samples from multicore GeoB9501-4 (Supplementary

Figure 3). Bulk samples were freeze-dried, powdered and homogenised. Single element concentrations were determined on 4g of dry subsamples by energy-dispersive polarisation X-ray fluorescence (EDP-XRF) spectroscopy using a Spectro Xepos instrument[41]. The instrument was operated by means of the software Spectro X-Lab Pro, Version 2.4, using the Turboquant method[42]. Analytical quality was assessed by repeated analyses of the certified standard reference material MAG-1[43]. The measured values were within 1% of the accepted value for Si, Al, K, Ca and Fe and within 2% for Ti. The standard deviation of replicates was less than 2%.

Calibration of the Avaatech XRF core scanner data

Element intensities were measured on gravity core GeoB9501-5 with an Avaatech XRF core scanner every 0.5 cm downcore as previously described[44]. Data from the XRF core scanner were calibrated by comparison to the element concentrations of the 53 powdered sediment samples taken along the length of the GeoB9501-5 core. In the original calibration method[45] a set of calibration equations are determined in log-ratio space by examining the regression relationships between the compositions obtained for powder samples measured on a calibrated XRF instrument and the XRF spectra measured on the scanner. The derived calibration equations are then applied to the scanner data across the entire core to yield elemental concentrations which take into account changes in specimen effects (including variable water content) and matrix effects. A detailed investigation revealed that such a global calibration was inappropriate in the case of core GeoB9501-5, thus an alternative local model was adopted. Calibration equations, typically spanning ~40 cm, were determined and applied in a piecewise manner through the core (the exact local domain size depending on the spacing of the reference samples). In order to compensate for slight depth mismatches between the scanner and powder measurement data sets, the scanner data were smoothed using a moving average filter in log-ratio space with a span of 5 cm. The final calibration, however, was applied to the unsmoothed scanner data.

Determination of dust, riverine and marine mass accumulation rates

In order to evaluate the relative abundances of aeolian, fluvial and marine material in the GeoB9501 sediments an end-member unmixing analysis was performed[46]. *End-member analysis* aims to provide a simplified low-rank approximation of a data set in terms of invariant parts. For this study, which involves a collection of sediment elemental compositions, end-members represent a small number of fixed compositions that when mixed together in various proportions can reproduce the measured data set.

To construct the mixing model four different matrices must be defined, $\boldsymbol{X}$, $\boldsymbol{A}$, $\boldsymbol{S}$ and $\boldsymbol{\varepsilon}$. The measured data can be placed in a matrix $\boldsymbol{X}$, which is composed of n rows, one for each sediment sample, and l columns spanning the suite of elements to be included in the analysis. The compositions of the end-members are based on measured data (see below) and define the matrix $\boldsymbol{S}$, which has m rows, one for each end-member and l columns spanning the same elements as the data in $\boldsymbol{X}$. It is important that each row of $\boldsymbol{X}$ and $\boldsymbol{S}$ is normalized to sum to one, this does not imply that the studied sediments and end-members contain no other elements than those selected in the analysis, but instead it creates a consistent normalized data structure where the relative abundances of the elements in a given sample are preserved. The unknown relative abundances of the end-members are held in the matrix, $\boldsymbol{A}$, again with n rows (one for each of the measured samples) and m columns (one for each end-member). Finally, there will always be differences between the measured and modelled data, these "errors" can be held in the matrix $\boldsymbol{\varepsilon}$ which will have the same size as $\boldsymbol{X}$, n by l. Given these definitions the linear mixing model can be represented in matrix notation as:

$$\boldsymbol{X} = \boldsymbol{A}\boldsymbol{S} + \boldsymbol{\varepsilon}$$

This mixing model acts to link one set of observations, the input end-members in $\boldsymbol{S}$, to the measured samples under investigation in $\boldsymbol{X}$. In the case of the above mixing equation, this linking model is $\boldsymbol{A}$, the relative abundances of the end-members in each sample, which can be found simply by solving a constrained least squares problem (see below).

Candidate *dust* and *fluvial* end-members were constructed using the normalized relative abundances of Si, Al, Ti, K and Ca from modern aeolian[47] (nine samples) and riverborne[48] material (ten samples). Note that although it was included in the elemental calibration procedure, Fe was not included in the unmixing analysis because of concerns over its possible mobility resulting from redox processes. As an example of the method, to construct one realization of the *dust* end-member a combination of nine samples was selected from the aeolian data set by a bootstrap with replacement routine (where "replacement" indicates that a given sample can be selected more than once in any single realization). The *dust* end-member was then represented by the central composition of the nine selected samples, determined using the additive log-ratio approach[49]. The composition of the *marine* end-member was based on measurements of opal at selected points in the GeoB9501 record to assess the biogenic Si content (Supplementary Table 2) and the assumption across the five selected elements that biogenic Ca would be by far the most abundant whilst the content of Al, Ti and K would be effectively zero[50]. On this basis the *marine* end-member was constructed as having a normalized relative composition of 2% Si and 98% Ca. To reiterate the ideas discussed above, this composition does not imply that the marine component will be composed solely of Si and Ca, because organic carbon, for example, could be expected to make a contribution. Instead the 2% Si and 98% Ca represents the normalized relative composition across the suite of five elements (Si, Al, Ti, K and Ca) included in the unmixing model. Numerical experiments showed that long-term evolution of the record was insensitive to small changes in the assumed *marine* end-member composition, with less than a 0.5% average change in the calculated abundance of the *marine* end-member when the Si contribution was changed from 0 to 5%.

The construction of end-members in the above manner assumes that their composition was approximately constant during the investigated period. It is however important to consider possible violations to this assumption, for example, the primary source area of the aeolian material may have shifted through time. By taking into consideration the composition of aeolian and riverine material over a wide geographical region and constructing spectra of end-member compositions via bootstrapping we aim to incorporate variability due to the

possibility of shifting source areas into the uncertainty of the unmixing results. In turn, this uncertainty can subsequently be propagated into the calculation of mass accumulation rates.

Given bootstrapped realizations of the *dust* and *fluvial* end-members and the constructed *marine* end-member, their relative abundance in the sediment was determined using non-negative least squares applied to each calibrated XRF core scanner composition to provide an estimate of $\boldsymbol{A}$ via the presented mixing equation. This analysis was performed using the SeDuMi optimization package[51] with the additional constraints that each contribution must be non-negative and the combined contributions of the *dust*, *fluvial* and *marine* end-members must sum to 100%. The supervised unmixing procedure was repeated with 500 different realizations of the end-members. The mean end-member relative contributions were calculated as a function of age using the additive log-ratio approach[49] which takes into account the relative and constrained nature of the data. In order to provide an appreciation of the variability introduced into the unmixing procedure by the bootstrapping, the minimum and maximum relative contributions obtained over the assemblage of 500 unmixing models were used to define an uncertainty envelope as a function of age.

Dry bulk density was determined by weighing wet samples and subsequently freeze-drying and re-weighing samples every 2 cm downcore in gravity core GeoB9501-5 and every cm in multicore GeoB9501-4. To determine the mass accumulation rates (expressed in g cm^{-2} yr^{-1}) of the three end-members their mean relative contributions were multiplied by the product of the sedimentation rate and the dry bulk density interpolated at the sample depths. An error envelope was constructed by repeating this procedure for the relative contributions obtained for all 500 unmixing models and propagating in the 2σ error for the sedimentation rate. From the distribution of results at each given depth interval the 2.5^{th} and 97.5^{th} percentiles were defined to provide a 95% nonparametric error envelope (shaded regions in Supplementary Figure 2).

Supplementary Notes

Determination of mass accumulation rate derivatives

Cubic smoothing splines[52] were employed to approximate each of the *dust*, *riverine* and *marine* mass accumulation rate curves. The level of smoothing was selected to capture the long-term evolution of the record whilst removing the higher frequency variability. The derivative of each spline was calculated directly from its coefficients (Supplementary Figure 4). An error envelope was constructed by repeating this procedure for the mass accumulation rates obtained from all 500 realizations of the unmixing procedure. The 2.5th and 97.5th percentiles were determined from the distribution of derivative curves for each component at each time interval to provide a 95% nonparametric error envelope.

Outlier analysis of the mass accumulation rate data

According to their ages, data from the dust, riverine and marine mass accumulation rates were assigned to bins 100 years in width. The median value of the data within each bin was determined and the standard error on the median was estimated[53]. To test for a changing relationship between the dust, riverine and marine mass accumulation rates the robust Mahalanobis distance[54] of each age interval was determined with respect to the group of all age intervals on the basis of the estimated covariance structure of the binned data[55] (Supplementary Figure 5). Thus, the Mahalanobis distance considers the covariance of the data, taking into account correlations whilst being scale invariant. Outlying bins were defined by a cut-off value representing the 97.5% tolerance level obtained from a chi-squared distribution with three degrees of freedom[56]. Bins with distances greater than the cut-off limit of $\sqrt{\chi^2_{3,0.975}}$ can be said to demonstrate atypical behaviour with respect to the robust covariance structure of the data. A 95% error envelope for the robust Mahalanobis distances was determined by numerical propagation of the standard error on the median of each bin. Based on the cut-off value, the 2 youngest bins (centred at 1850 and 1950 CE) can be deemed to be outlying. It is thus apparent that the relationship between the dust, riverine and marine

mass accumulation rates at the core location changed fundamentally at some time around 1750-1850 CE.

Correlation between mass accumulation rates and Lake Bosumtwi $\delta^{18}O$

To investigate the relationship between the reconstructed mass accumulation rates and the Lake Bosumtwi $\delta^{18}O$ record a correlation analysis was performed using the software PearsonT[57] which takes into account the serial dependence and non-normal distribution of the signals. For this purpose we resampled the higher-resolution mass accumulation rate records at the ages of the lower-resolution Lake Bosumtwi $\delta^{18}O$ time series using linear interpolation and then detrended each record (including Lake Bosumtwi) linearly. For the time interval 700 BCE to 1700 CE (n=291) Pearson's *r* is 0.40 with a 95%- confidence interval [0.19; 0.60] for $\delta^{18}O$ vs. aeolian flux, 0.39 [0.25; 0.52] for $\delta^{18}O$ vs. riverine flux and 0.51 [0.26; 0.61] for $\delta^{18}O$ vs. marine flux.

Comparison of dust fluxes at Site GeoB9501 to sediment trap data

Sediment trap studies off NW Africa show that the seasonal dust input is reflected in the lithogenic flux in the water column[58]. The observed dust flux in those traps is around 0.0022 g cm^{-2} yr^{-1} and hence by a about factor 50 to 70 lower than observed for the years 1984 to 1988 at Site GeoB9501. However, we have to take into account that the dust flux strongly decreases with increasing distance from the coast[59]. The nearest sediment trap site is about 500 km west of the African coast (Eumeli Site, Ref. 58). Site GeoB9501 is located about 30 km to the west of Mauritania and in close proximity to dust sources on land. Dust fluxes at observatories in Dakar[60] and Malé[61] are about 0.021g cm^{-2} yr^{-1} (mean flux 1984-1988) and 0.031g cm^{-2} yr^{-1} (based on measurements in the time from 01.07.2005 to 30.09.2005) and hence still a factor of 3-5 lower than at site GeoB9501. Recently, however, it has been shown[62] that the catch efficiency of the CAPYR (capteur pyramidal) dust sampler used in the studies[60,61] mentioned above underestimates the dust deposition by a factor of about 2-5 with respect to other techniques and further with respect to deposition on a water surface, where no resuspension is possible. We thus conclude that the relatively high dust fluxes recorded at Site

GeoB9501 are not inconsistent with available dust-flux measurements at the nearest observatories in Africa in Dakar and Malé.

Note on River Fluxes

Although Senegal sediment discharge generally increases with water discharge[63] it is very likely that human influence and vegetation cover along the Senegal River also had a considerable influence on the total sediment load of the Senegal River due to erosional processes along the river. An increasing amount of water erosion structures (i.e., backward erosion, gullying, bank erosion) due to anthropogenic pressure on the vegetation cover has actually been observed along the Senegal River[64] during the past 10 years. This explains why the accumulation rate of fluvial material also increased along with the increased land use (Supplementary Figure 2).

Note on Marine Fluxes

The reconstructed marine flux increases along with the dust flux increase during the past 300 years (Supplementary Figure 2). A covariation of biogenic and lithogenic fluxes has also been observed in sediment trap studies. For example in the Cape Blanc area, the flux of lithogenic components is tightly related to marine components[65] as organic carbon, carbonate and opal. This covariation can be explained by the Ballast-Effect[66], the increase of the excess density of settling particles through lithogenic material which causes a faster and more efficient transfer of marine components to the sea floor.

References

31 Appleby, P. G. & Oldfield, F. The calculation of lead-210 dates assuming a constant rate of supply of unsupported ^{210}Pb to the sediment. *Catena* **5**, 1-8 (1978).

32 Pittauerová, D. *et al.* Application of self-absorption correction method in gamma spectroscopy for ^{210}Pb and ^{137}Cs sediment chronology on the continental slope off NW Africa. *Radioprotection* **44**, 457–461 (2009).

33 McGregor, H. V., Dima, M., Fischer, H. W. & Mulitza, S. Rapid 20th-century increase in coastal upwelling off northwest Africa. *Science* **315**, 637-639 (2007).

34 Hurtado, S., Villa, M., Manjo, G. & Garcia-Tenorio, R. A self-sufficient and general method for self-absorption correction in gamma-ray spectrometry using GEANT4. *Nucl. Instrum. Methods A* **580**, 234-237 (2007).

35 Bronson, F. L. Validation of the accuracy of the LabSOCS software for mathematical efficiency calibration of Ge detectors for typical laboratory samples. *J. Radioanal. Nucl. Chem.* **255**, 137-141 (2003).

36 Franke, J., Paul, A. & Schulz, M. Modeling variations of marine reservoir ages during the last 45 000 years. *Clim. Past* 4, 125-136 (2008).

37 Gubbins, D. *Time Series Analysis and Inverse Theory for Geophysicists*. (Cambridge University Press, 2004).

38 Teanby, N. A. Constrained smoothing of noisy data using splines in tension. *Math. Geol*. **39**, 419-434 (2007).

39 Müller, P. J. & Schneider, R. An automated leaching method for the determination of opal in sediments and particulate matter. *Deep-Sea Res. I* **40**, 425-444 (1993).

40 Mulitza, S. *et al.* Sahel megadroughts triggered by glacial slowdowns of Atlantic meridional overturning. *Paleoceanography* **23**, PA4206 (2008).

41 Wien, K., Wissmann, D., Kölling, M. & Schulz, H. D. Fast application of X-ray fluorescence spectrometry aboard ship: how good is the new portable Spectro Xepos analyser? *Geo-Mar. Lett.* **25**, 248–264 (2005).

42 Schramm, R. & Heckel, J. Fast analysis of traces and major elements with ED(P)XRF using polarized X-rays: TURBOQUANT. *J. Phys. IV* **8**, 335–342. (1998).

43 Govindaraju, K. 1994 compilation of working values and descriptions for 383 geostandards. *Geostandards Newslett.* **18**, 1–158 (1994).

44 Tjallingii, R., Röhl, U., Kölling, M. & Bickert, T. Influence of the water content on X-ray fluorescence core-scanning measurements in soft marine sediments. *Geochem. Geophys. Geosyst.* **8**, Q02004 (2007).

45 Weltje, G. J. & Tjallingii, R. Calibration of XRF core scanners for quantitative geochemical logging of sediment cores: Theory and application. *Earth Planet. Sci. Lett.* **274**, 423-438 (2008).

46 Ehrlich, R. & Full, W. E. Sorting Out Geology – Unmixing Mixtures, in *Use and Abuse of Statistical Methods in Earth Sciences* (ed W. Size) 33–46 (Oxford University Press, 1987).

47 Moreno, T. *et al.* Geochemical variations in aeolian mineral particles from the Sahara-Sahel Dust Corridor. *Chemosphere* **65**, 261-270 (2006).

48 Gac, J. Y. & Kane, A. Le fleuve Sénégal: I. Bilan hydrologique et flux continentaux de matières particulaires à l'embouchure. *Sci. Géol. Bull.* **39**, 99–130 (1986).

49 Aitchison, J. Measures of location of compositional data sets. *Math. Geol*. **21**, 787-790 (1989).

50 Schulz, H. D. & Zabel, M. *Marine Geochemistry.* (Springer, 2006).

51 Sturm, J. F. Using SeDuMi 1.02, a MATLAB toolbox for optimization over symmetric cones. *Optim. Method Softw.* **11**, 625-653 (1999).

52 de Boor, C. *A Practical Guide to Splines*. (Springer, 1978).

53 Sachs, L. *Angewandte Statistik*. (Springer, 2002).

54 Maronna, R., Martin, R. D. & Yohai, V. J. *Robust statistics: theory and methods*. (Wiley, 2006).

55 Filzmoser, P. & Hron K. Outlier detection for compositional data using robust methods. *Math. Geosci.* 40, 233-248 (2008).

56 Rousseeuw, P. J. & van Zomeren, B. C. Unmasking multivariate outliers and leverage points. *J. Am. Stat. Assoc.* **85**, 633-651 (1990).

57 Mudelsee, M. Estimating Pearson's correlation coefficient with bootstrap confidence interval from serially dependent time series. *Math. Geol*. **35**, 651-665 (2003).

58 Bory, A. J. M. & Newton, P. P. Transport of airborne lithogenic material down through the water column in two contrasting regions of the eastern subtropical North Atlantic Ocean. *Glob. Biogeochem. Cycles* **14**, 297-315 (2000).

59 Goudie, A. S. & Middleton, N. J. Saharan dust storms: nature and consequences. *Earth-Sci.Rev.***56**, 179-204 (2001).

60 Orange, D. & Gac, J. Y. Bilan géochimique des apports atmosphériques en domaines sahélien et soudano-guinéen d'Afrique de l'Ouest (bassins supérieurs du Sénégal et de la Gambie). *Géodynamique* **5**, 51-55 (1990).

61 Gassani, J., Bent Mohamed, A., Duchesne, J. & Ozer, P. Preliminary results of Saharan dust deposition during the rainy season 2005 in Mâle (Southern Mauritania). *Geo-Eco-Trop* **29**, 69-76 (2005).

62 Goossens, D. & Rajot, J. L. Techniques to measure the dry aeolian deposition of dust in arid and semi-arid landscapes: a comparative study in West Niger. *Earth Surf. Proc. Land.* **33**, 178-195 (2008).

63 Kattan, Z., Gac, J. Y. & Probst, J. L. Suspended sediment load and mechanical erosion in the Senegal Basin - estimation of the surface runoff concentration and relative contributions of channel and slope erosion. *J. Hydrol.* 92, 59-76 (1987).

64 Niang, A. J., Ozer, A. & Ozer, P. Fifty years of landscape evolution in Southwestern Mauritania by means of aerial photos. *J. Arid Environ.* 72, 97-107 (2008).

65 Fischer, G. *et al.* Mineral ballast and particle settling rates in the coastal upwelling system off NW Africa and the South Atlantic. *Int. J. Earth Sci.* **98**, 281-298 (2009).

66 Armstrong, R. A., Peterson, M. L., Lee, C. & Wakeham, S. G. Settling velocity spectra and the ballast ratio hypothesis. *Deep-Sea Res. II* **56**, 1470-1478 (2009).

Supplementary Figures

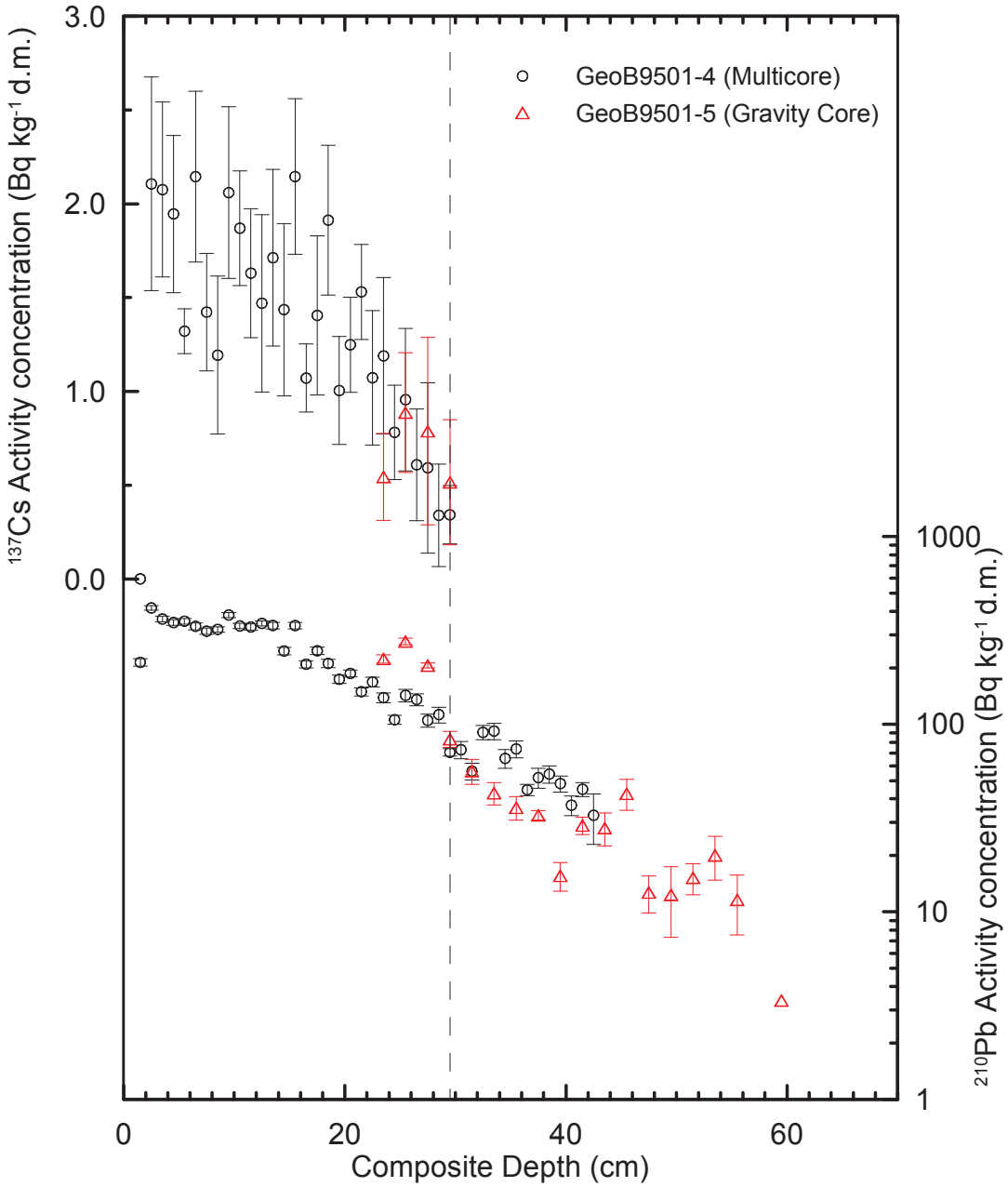

Supplementary Figure S1 Matched multicore (circles) and gravity core (triangles) depth profiles of activity concentrations of ^{137}Cs and ^{210}Pb$_{xs}$ ($\log_{10}$ scale) in sediment dry mass (d.m.). About 21.5 cm of sediment have been lost during coring. All sampling depths in gravity core GeoB9501 have been corrected by +21.5 cm.

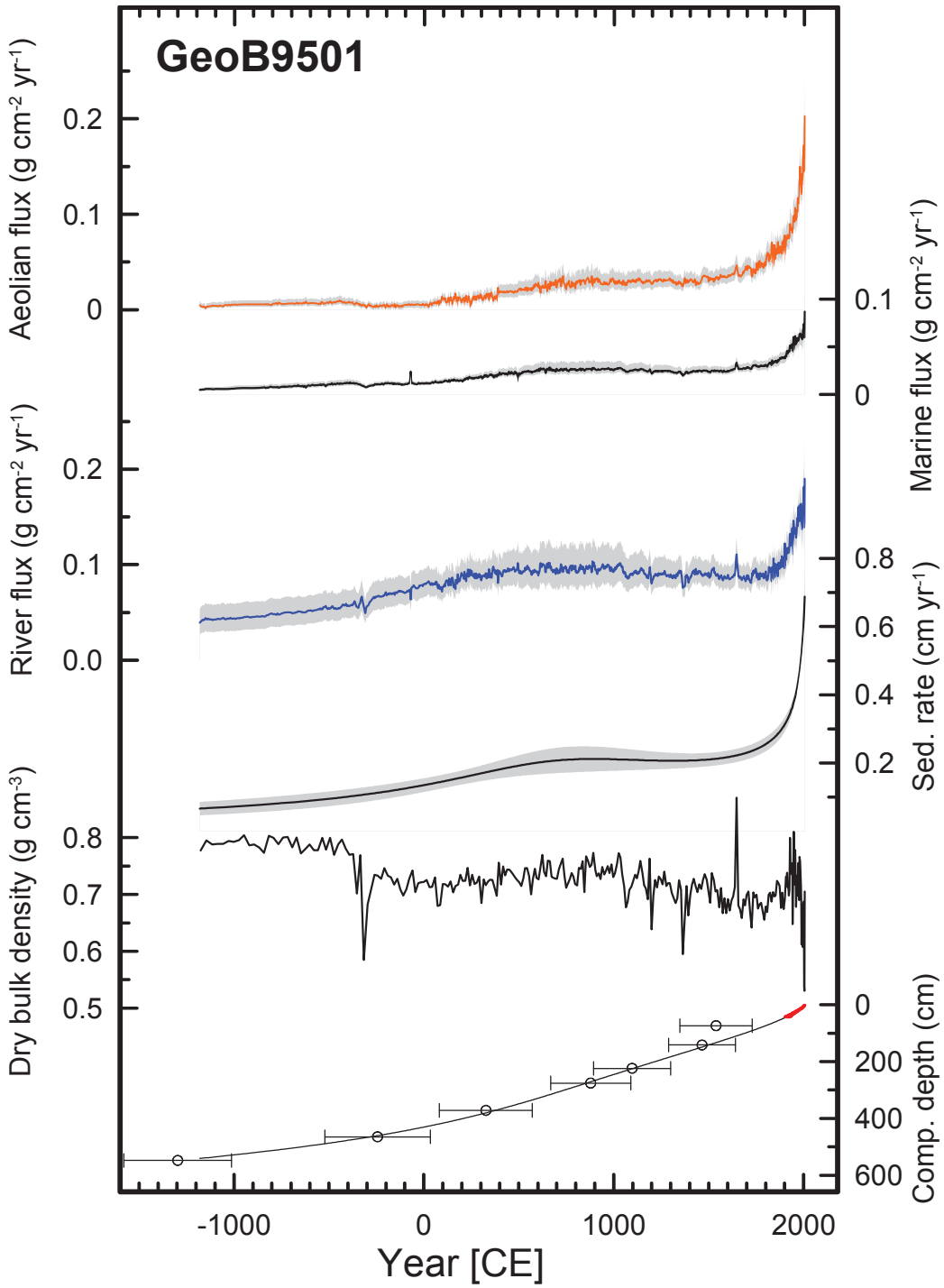

Supplementary Figure S2 Accumulation rates of aeolian, riverine and marine material in addition to total sedimentation rate, dry bulk density and modelled age-depth relation for Site GeoB9501. Grey shading indicates 95% nonparametric error envelope for flux estimations and 2σ error envelope for sedimentation rate. Error bars indicate 2σ age range for the conversion of radiocarbon ages into calibrated calendar years. Red line indicates 2σ error envelope of $^{210}Pb_{xs}$-based age model.

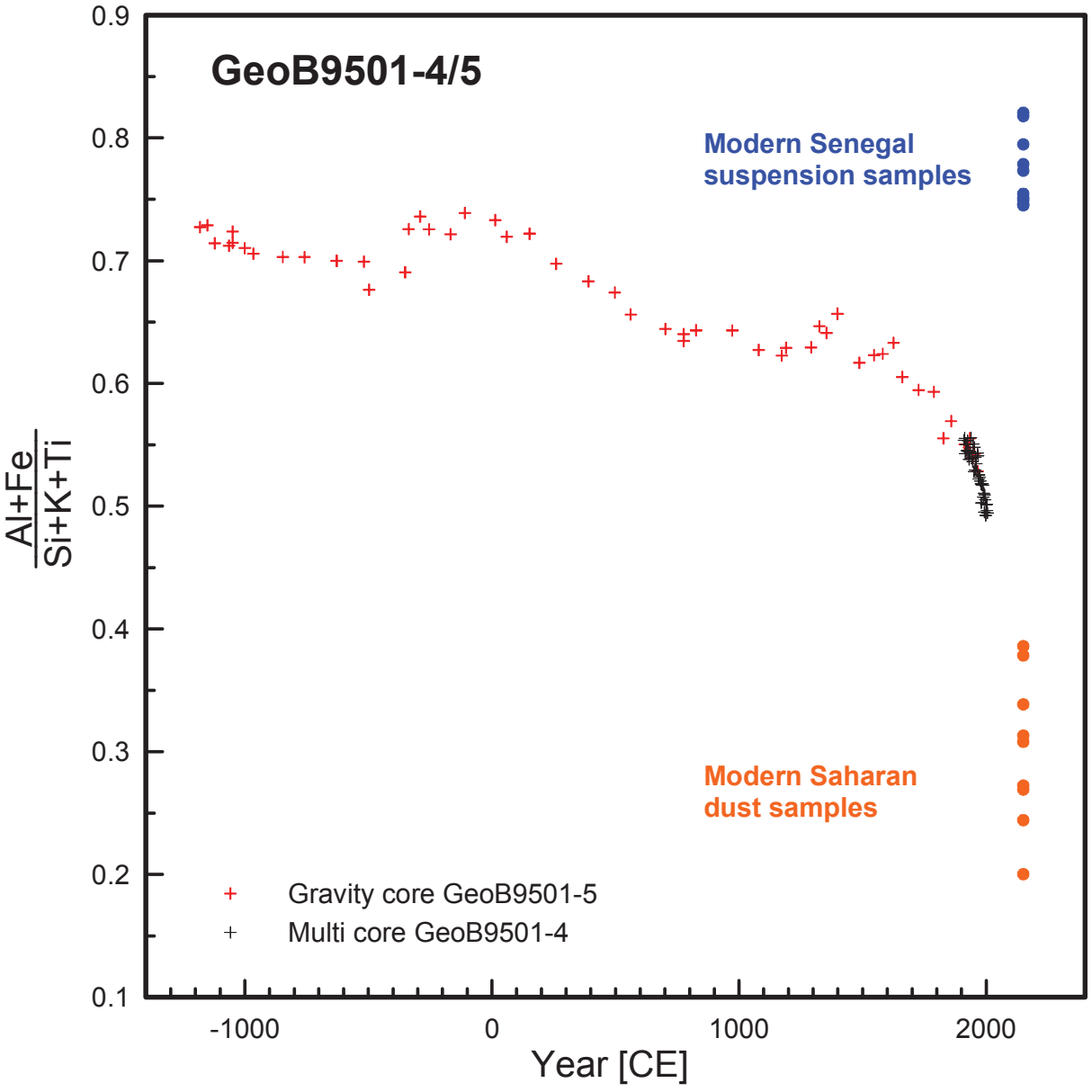

Supplementary Figure S3 Downcore variation of the ratio (Al+Fe)/(Si+K+Ti), measured on powdered bulk sediment samples of multi corer GeoB9501-4 (black crosses) and gravity corer GeoB9501-5 (red crosses). Bulk samples have been used to calibrate XRF scanner measurements. (Al+Fe)/(Si+K+Ti) ratios of nine modern aeolian samples[47] (orange dots) and ten Senegal suspension samples[48] (blue dots) have been used to constrain the modern endmember compositions of atmospheric dust and riverborne sediments.

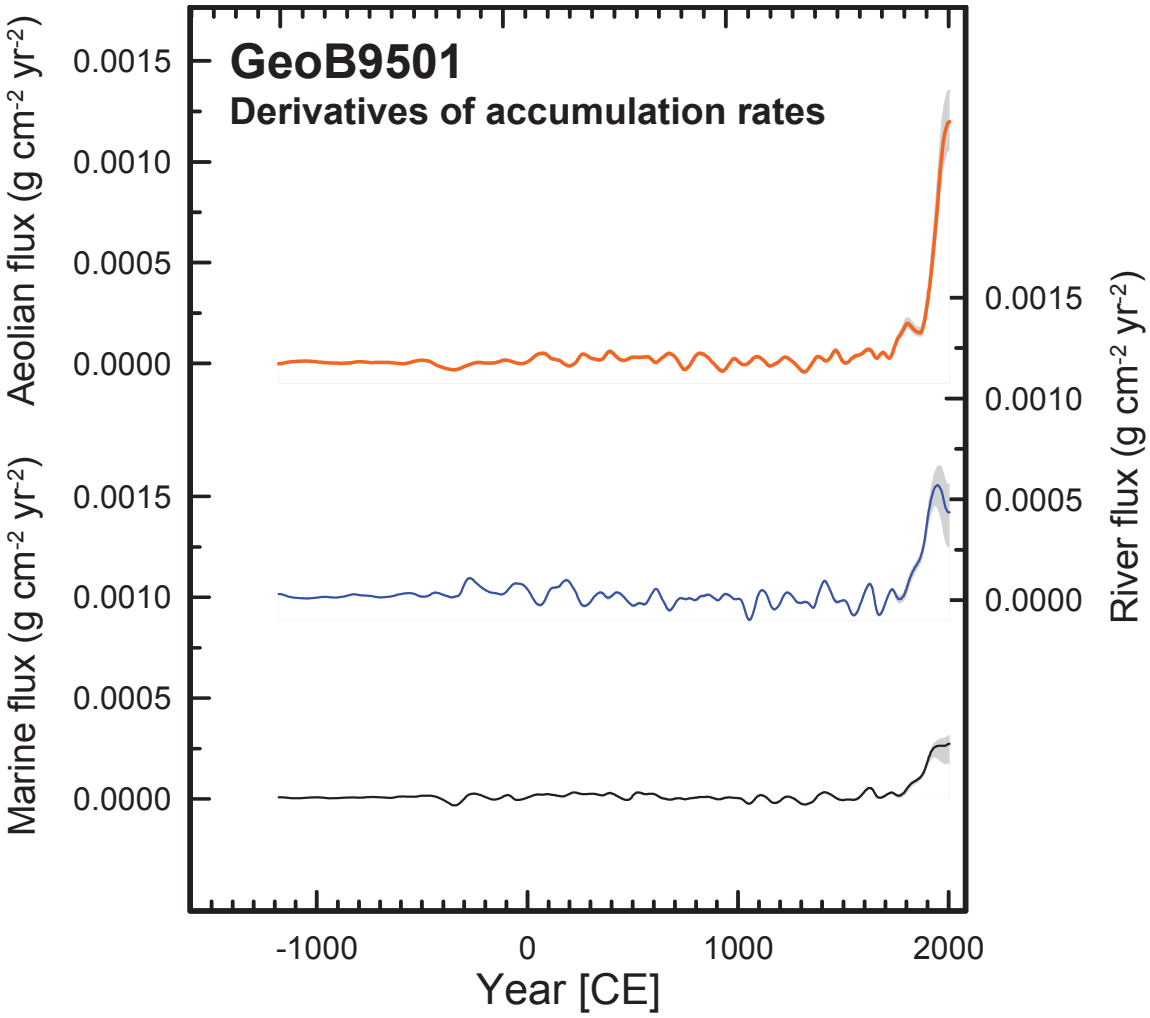

Supplementary Figure S4 Derivatives of deposition flux rates of aeolian, riverine and marine matter.

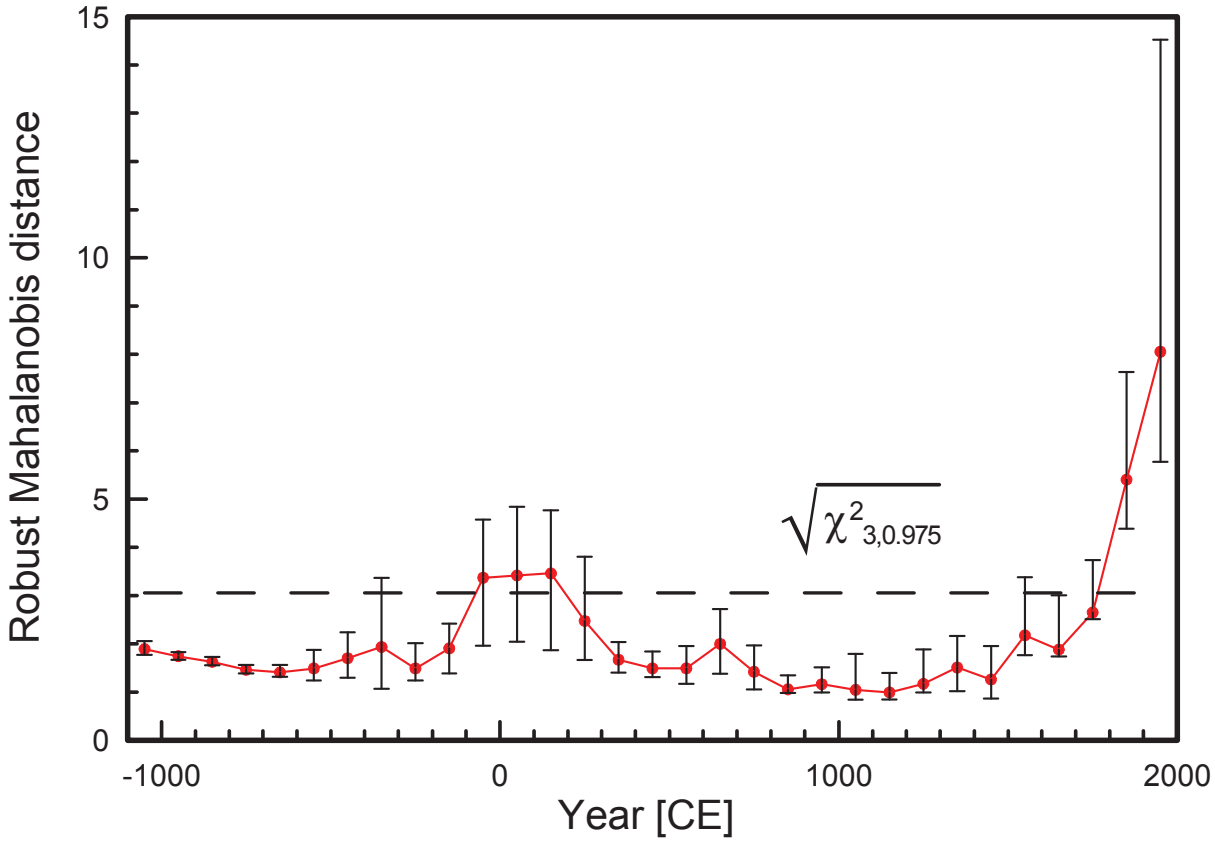

Supplementary Figure S5 The robust Mahalanobis distances of the binned GeoB9501 mass accumulation rate data. A cut-off value (dashed line) with which to define outlying points was obtained from a chi-squared distribution at the 97.5% quantile with three degrees of freedom. The error bars on the individual time points represent the 95% error envelope obtained by numerical propagation of the standard errors on the bins into the distance calculation. The two youngest bins, positioned at 1850 and 1950 CE, can be deemed to be outlying.